Electronic Supplementary Information

A semiconductor junction photoelectrochemical device without a depletion region

Jin-Young Jung, Sung-Hae Kim, Sambhaji S. Shinde, Dong-Hyung Kim, Chao Lin, and Jung-Ho Lee*

Department of Materials Science and Chemical Engineering, Hanyang University, 55 Hanyangdaehak-ro, Sangnok-gu, Ansan, Kyeonggi-do 15588, Republic of Korea

E-mail: jungho@hanyang.ac.kr

Experimental Section

Fabrication of Ni thin film/SiO_2/Si photoelectrodes: Single-crystalline p- and n-type Si (100) wafers of ~1–10 Ω·cm were used as photocathodes and photoanodes, respectively. Degenerately doped n^+- and p^+-type Si (100) wafers with resistivities of 0.001–0.002 Ω·cm were also used to characterize the charge-transfer kinetics and the electrochemical charge capacitance. Before deposition of a metal thin film, Si wafers were dipped into dilute hydrofluoric acid (HF) to remove the native oxide, and then rapid thermal oxidation (RTO) was performed at 900 °C under atmospheric conditions to grow a thin SiO_2 layer on the Si surface. Ni thin films were deposited by an electron-beam evaporation process based on a high-vacuum pressure of ~10^{-6} Torr at a deposition rate of ~0.2 Å/s. The back sides of the Si wafers were contacted with an In–Ga eutectic alloy (Sigma-Aldrich). Other thin film materials, including Ni, Fe, Co, Ti, and NiO_x, were also deposited by evaporation.

Characterization of the Ni thin films: the morphologies and elemental composition of the deposited Ni thin films were characterized by high-resolution transmission electron microscopy (HRTEM, JEOL, JEM-2100F, Japan) equipped with energy-dispersive X-ray spectroscopy (EDXS) at an accelerating voltage of 200 kV. The thickness of the deposited Ni thin film was verified by cross-sectional TEM images. The chemical states of the Ni thin films were investigated by X-ray photoelectron spectroscopy (XPS) equipped with a monochromatic Al Kα (1.486 eV) source.

PEC characteristics of the Si photocathodes: PEC cells were assembled by a homemade Teflon bath, and PEC tests were performed using a potentiostat (Iviumstat) with a three-electrode configuration, including the Si photoelectrodes, a saturated calomel reference electrode, and a Pt mesh counter electrode. Key PEC performances were measured in 1 M KOH electrolyte. The electrolyte pH-dependent PEC performances were characterized in a 0.5 M Na_2SO_4 solution by adding 1 M KOH or 0.5 M H_2SO_4. CV and LSV responses were measured under various illuminations of 10–100 mW/cm^2 (using a Xe lamp with an AM 1.5 filter) and at various scan rates of 50–300 mV/s to observe the PEC responses. Chronopotentiometry methods under chopped illumination at open circuit conditions and under illumination at –10 mA/cm^2 were used to measure V_{ph} and stability, respectively. The

Mott–Schottky analysis was implemented in the frequency range of 2.5 MHz–1 Hz under dark conditions. The effective carrier lifetime was measured by quasi-steady-state photoconductance (QSSPC, WCT-120).

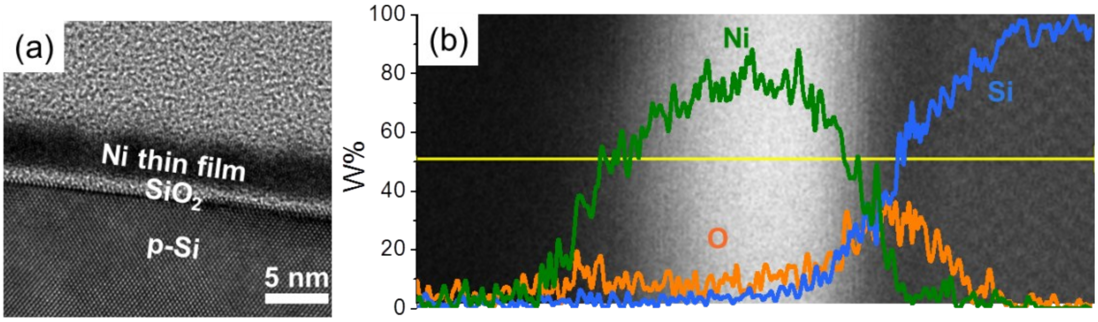

Fig. S1 (a) HRTEM image and (b) EDXS line profile of the 3-nm-thick ultrathin Ni film/SiO_2/p-Si photocathode.

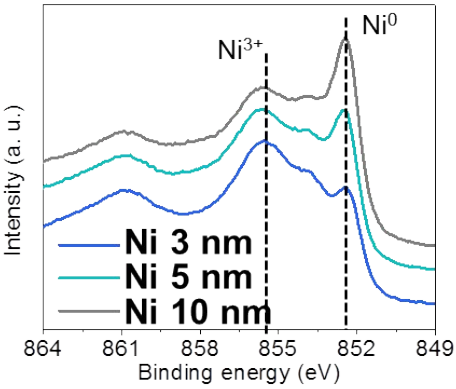

Fig. S2 Ni 2p XPS spectra of Ni thin films with thicknesses of 3 nm, 5 nm, and 10 nm.

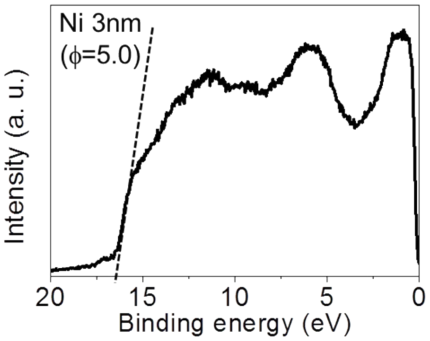

Fig. S3 Ultraviolet photoelectron spectroscopy characterizing the work function of 3-nm-thick ultrathin Ni film.

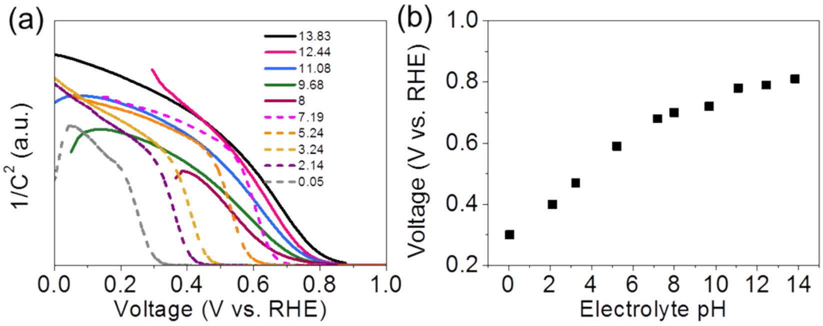

Fig. S4 (a) Mott-Schottky plots characterizing V_{fb} of a 5-nm-thick Ni thin film/SiO_2/Si photocathode at various electrolyte pH values. Starting with 0.5 M Na_2SO_4 electrolyte, the pH is adjusted by adding 1 M KOH (solid line) or 0.5 M H_2SO_4 (dotted line). (b) Plot denoting the V_{fb} results as a function of pH. The redox potential of the electrolyte shifts to the vacuum level as the pH increases such that V_{fb} of the 5 nm sample forming the mixed junction increases positively.

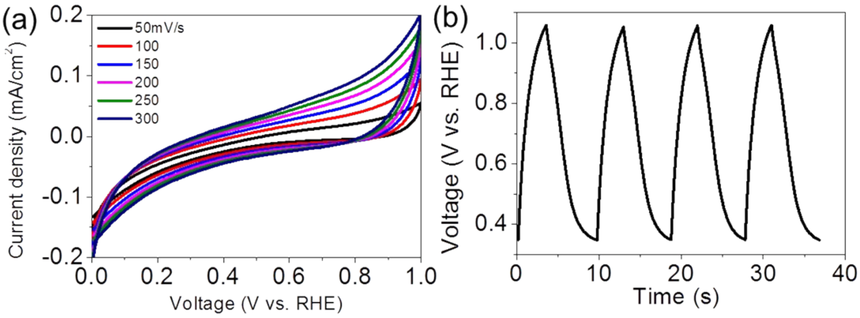

Fig. S5 Scan rate-dependent CV and GCD responses for the 3-nm-thick Ni thin film/SiO_2/n$^+$-Si sample. CV and GCD curves exhibit charge and discharge at the Ni surface through formation of an electrolytic capacitance layer (i.e., electric double layer).

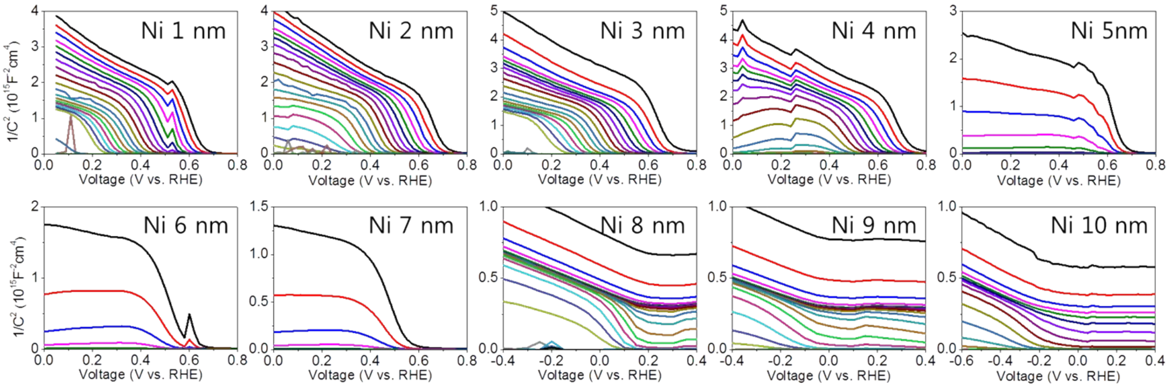

Fig. S6 Frequency-dependent Mott–Schottky plots for the Ni thin film/SiO_2/Si at various thickness of the thin film.

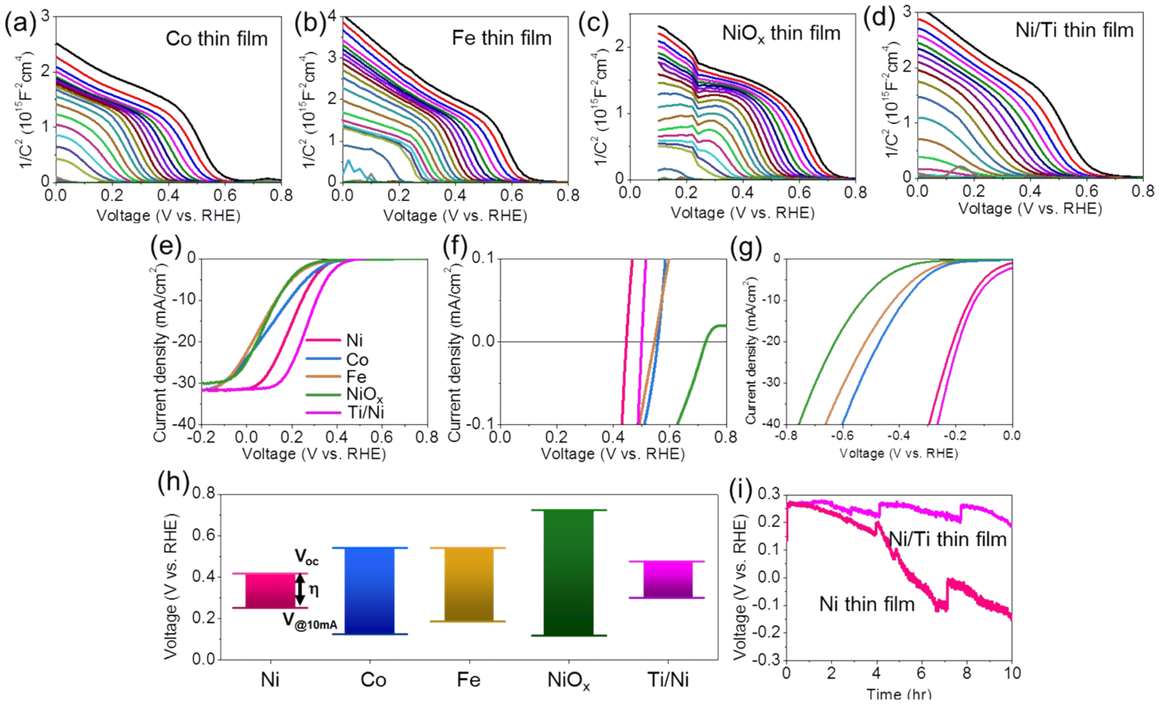

Fig. S7 Frequency-dependent V_{fb} of the Si photocathodes coated with ultrathin films of (a) Fe, (b) Co, (c) NiO_x, and (d) Ni/Ti. (e) Illuminated LSV curves of the Si photocathodes coated with 3-nm-thick ultrathin films of Ni, Co, Fe, NiO_x, and Ni/Ti. (f) V_{oc} and (g) η characteristics for Fe, Co, NiO_x, and Ni/Ti. (h) Plots describing the PEC performance of V_{oc}, η, and $V_{@10mA}$ for the various ultrathin film materials. (i) Stability test of the Ni and Ni/Ti samples at a photocurrent of 10 mA/cm^2.

The V_{fb} results for all ultrathin films were variable with frequency, indicating the application of the surface-active junction (Figure S7a-d). Among these ultrathin films, the Ni sample showed the best value of $V_{@10ma}$ (0.25 V) due to the lowest overpotential loss (0.17 V) of Ni for HER despite the lowest V_{oc} gain (0.42 V) (see Figure S7e-h). In contrast, as reported in our previous work, NiO_x achieved the highest V_{oc} of 0.75 V, but the high overpotential loss of 0.6 V limits $V_{@10ma}$. The thin film has been considered as a protection layer, but the sole Ni thin film does not ensure long-term stability. As a protection layer, we deposited a 1.5-nm-thick Ti film, followed by deposition of a 1.5-nm-thick Ni film. The Ti/Ni bilayer showed long-term stability at the highest $V_{@10ma}$ of 0.3 V (see Figure S7i).

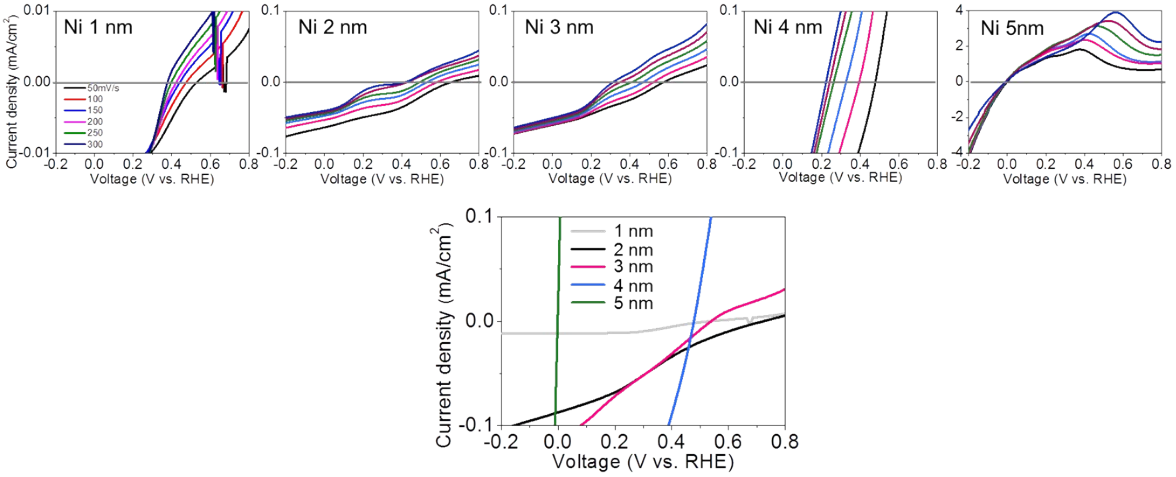

Fig. S8 Scan rate-dependent dark LSV curves for the Si photocathodes coated with various thicknesses of the Ni thin film. The bottom plot is a comparison of the dark LSV results at a scan rate of 50 mV/s. The potential at zero current shifts in the anodic direction as the thickness decreases due to dominance of the electrostatic potential charge at the capacitive surface.

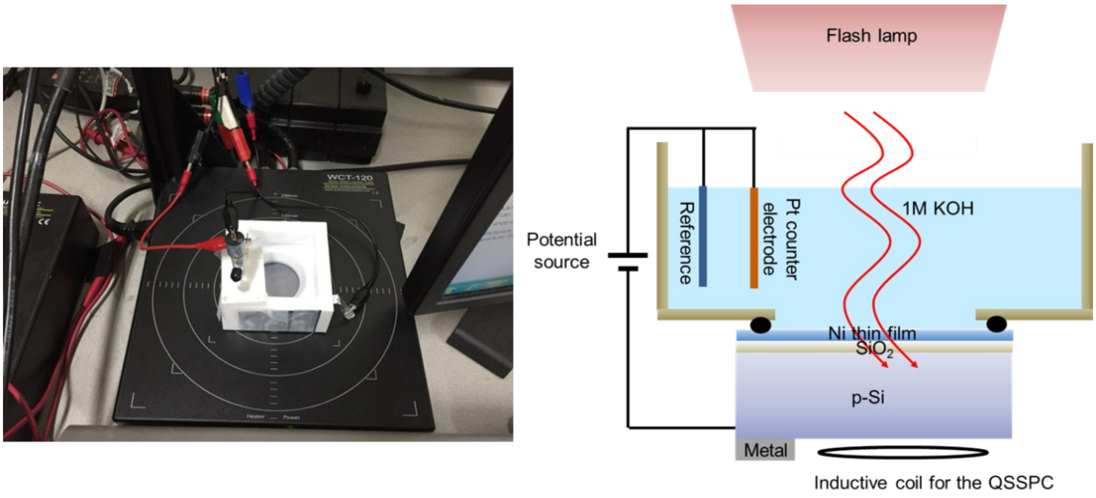

Fig. S9 Digital photo and schematic showing the minority carrier lifetime measurement system for the PEC cells under an applied potential.

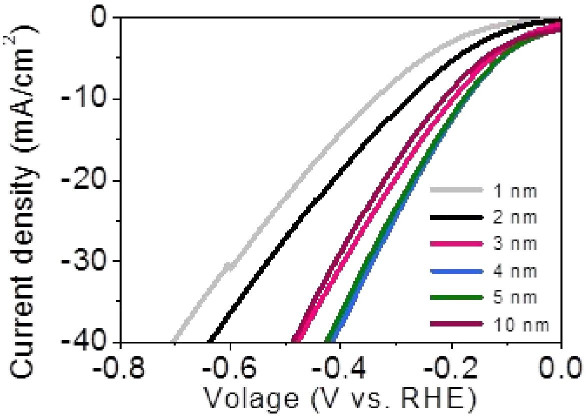

Fig. S10 LSV curves of the Ni thin film/SiO_2/n^+-Si samples to characterize the charge transfer kinetics at various thicknesses of Ni thin films.

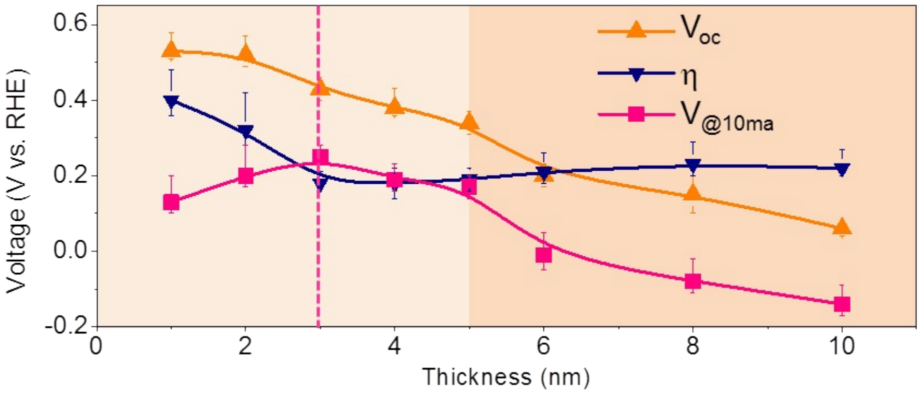

Fig. S11 The key parameters of V_{oc}, overpotential (η), and $V_{@10mA}$ as a function of thickness of the Ni thin films.

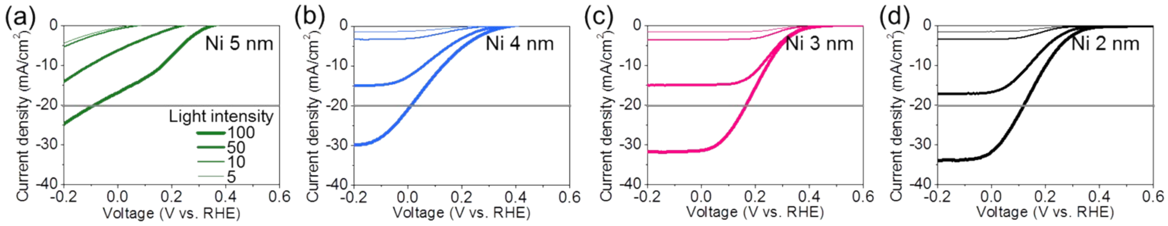

Fig. S12 Illuminated LSV curves of Ni thin film/SiO_2/Si photocathodes at various thicknesses of (a) 5 nm, (b) 4 nm, (c) 3 nm, and (d) 2 nm.

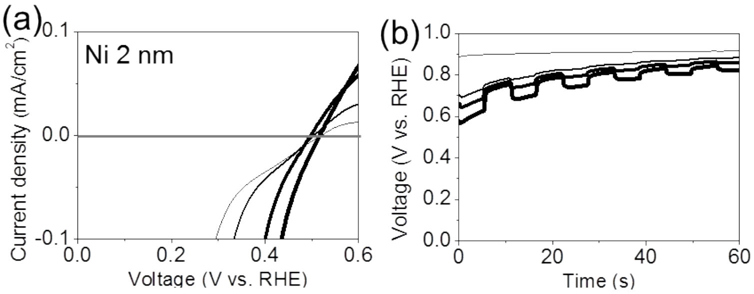

Fig. S13 (a) V_{oc} and (b) V_{ph} results of the 2-nm-thick Ni thin film/SiO_2/Si photocathode.

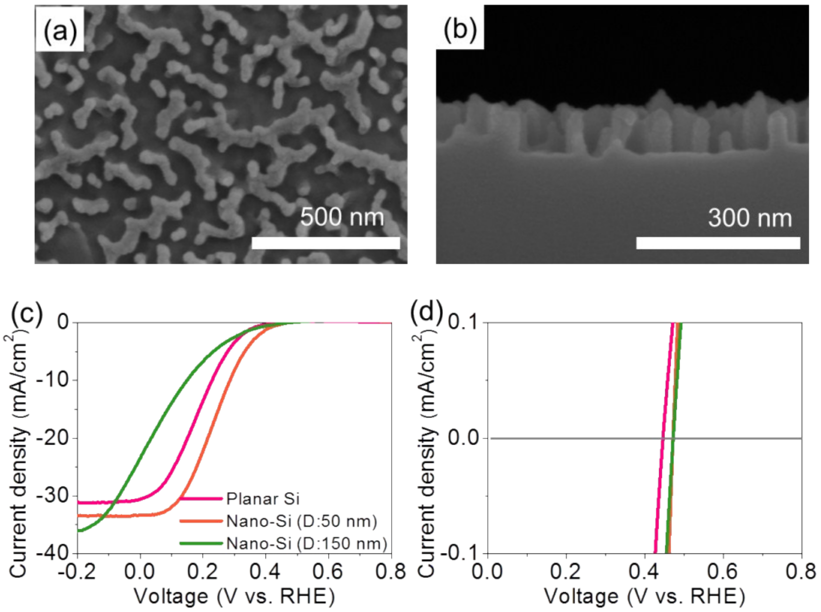

Fig. S14 (a) Top-view and (b) cross-sectional-view SEM images of the nanostructured Si. (c) Illuminated LSV curves for the 3-nm-thick Ni thin film/SiO_2/nanostructured Si photocathode with the surface-capacitive junction. (d) Low current level range of (c) for characterizing V_{oc}.

For the Schottky junction, V_{oc} is determined by V_{ph}, which is generated as a result of the thermodynamics of the light-induced charge carrier generation and recombination at the semiconductor. When employing the nanostructured Si photoelectrodes, the increase in nanostructure depth (surface area) suffers from larger surface recombination loss, leading to decrease in V_{ph} and thus V_{oc}. In contrast, for the surface-capacitive junction, V_{oc} is decoupled from V_{ph} so as to be irrelevant to the surface recombination loss. Therefore, V_{oc} is unchanged even for the increase in the depth (i.e., surface recombination loss). This clearly corroborates that V_{oc} of the surface-capacitive junction is not affected by the surface recombination losses as a result of decoupling. A detailed mechanical understanding of V_{oc} irrelevant to the thermodynamics of charge carriers is presented in the manuscript Ref. 40.

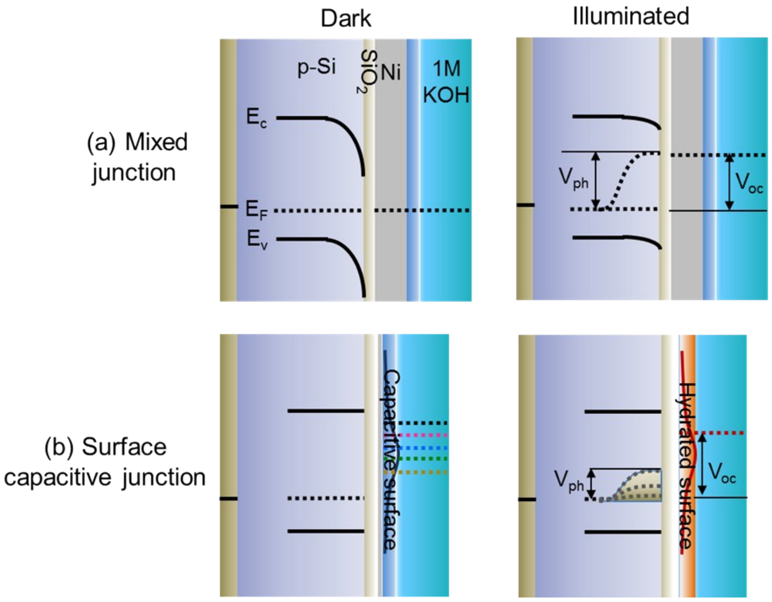

Fig. S15 The energy band diagrams for (a) the mixed junction and (b) the surface-capacitive junction under dark (left) and illuminated (right) conditions.

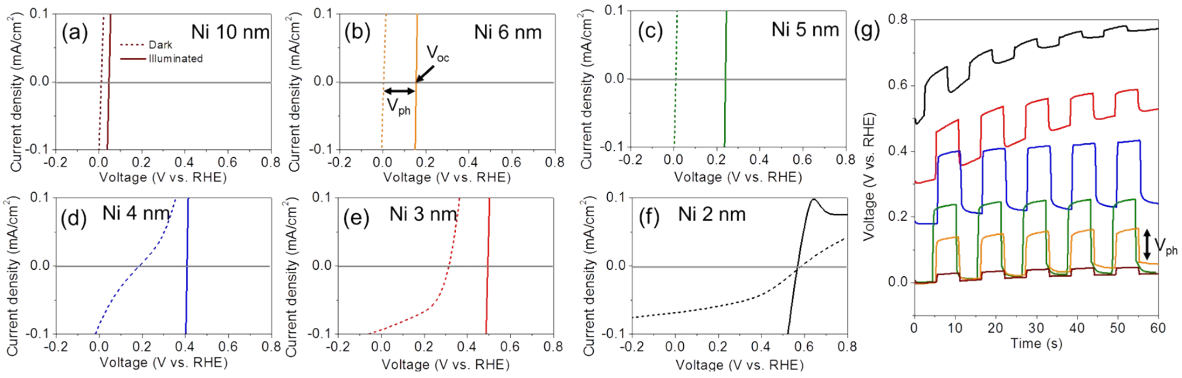

Fig. S16 (a-f) Dark and illuminated LSV curves at a low current-level range for characterizing the dependency of V_{oc} on V_{ph}. (g) The V_{ph} measurement by chronopotentiometry under chopped illumination in the open-circuit condition.

The dark curves for the buried and mixed junction (the Ni thickness of 5~10 nm) crossed over the zero point, and the illuminated curve shifted away from the dark curve by as much as the V_{ph} value (Figure S16a-c). In contrast, the surface-capacitive junction (2~4 nm) observed dark curves crossing over the non-zero point (Figure S16d-f). The shift degree of illuminated curve from the dark curve is not related to V_{ph}, and the V_{ph} value is dynamically changed during the measurement (see the black and red curves in Figure S16g). Interestingly, for the 4 nm sample that is located at the transition position between the surface-capacitive junction and the mixed junction, the crossing over non-zero point appears to form the surface-capacitive junction. However, the constant V_{ph} value (see the blue curve in Figure S16g) and splitting degree of the dark and illuminated curves corresponds well to V_{ph} (Figure S16d), suggesting the application of the photovoltaic principle as well.

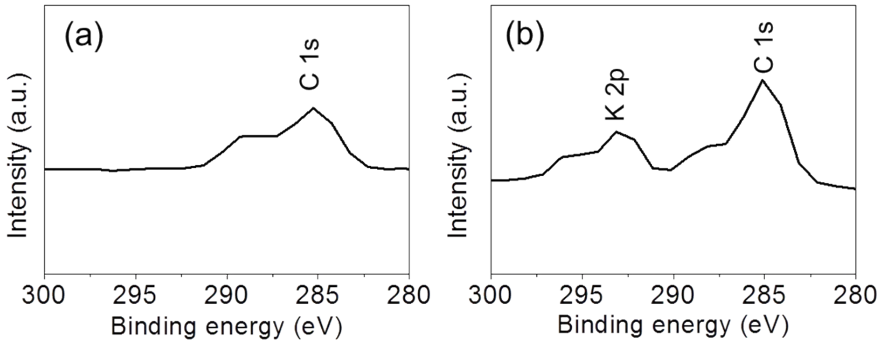

Fig. S17 K 2p XPS spectra of Ni thin films in (a) the pristine and (b) test samples after dark LSV responses for 5 cycles. The K 2p peak is newly observed after dark LSV responses due to K^+ ion adsorption at the Ni surface.

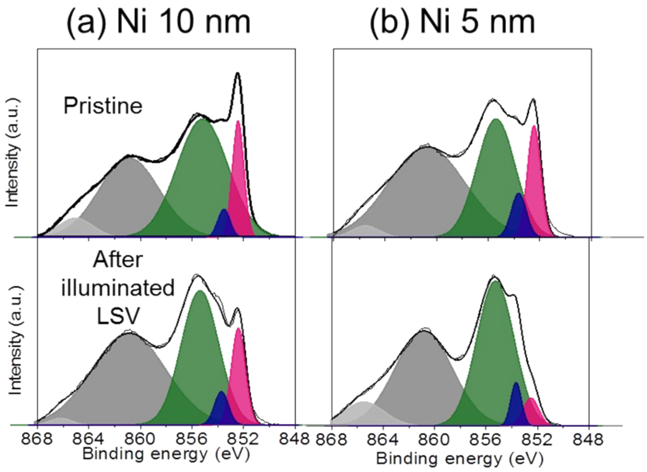

Fig. S18 Ni 2p XPS spectra of (a) 10-nm- and (b) 5-nm-thickness Ni thin films in (top) pristine and (bottom) test samples after illuminated LSV responses for 5 cycles.

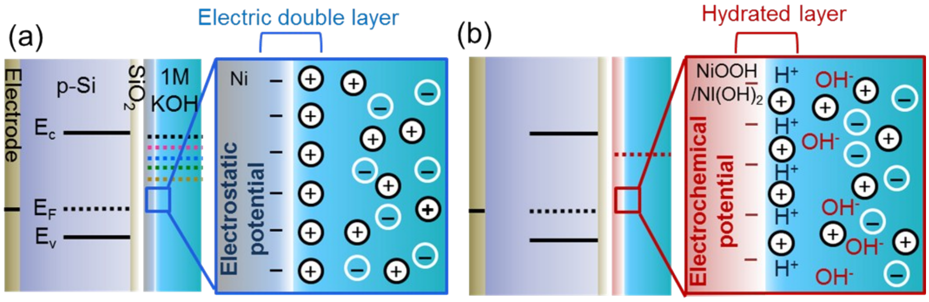

Fig. S19 Schematics describing the surface state of an ultrathin Ni film under (a) dark (electrostatic charge accumulation) and (b) illumination (electrochemical charge accumulation).

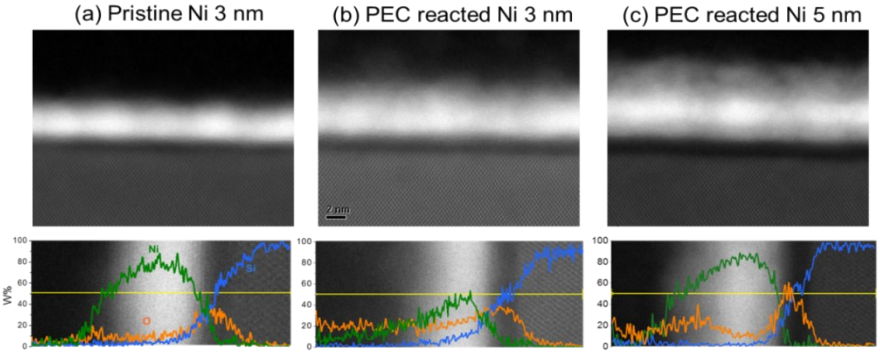

Fig. S20 (Top) STEM images and (bottom) EDSX line profiles for (a) the pristine sample, (b) PEC-reacted 3-nm-thick Ni thin film, and (c) PEC-reacted 5 nm-thick Ni thin film.

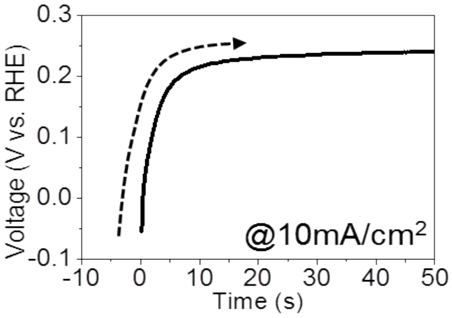

Fig. S21 Chronopotentiometry (potential change) measurement of the Ni thin film/SiO_2/Si photocathode at a photocurrent of 10 mA/cm^2.

The anodic shift resulted from reduction of kinetic overpotential, because V_{oc} is unchanged. The reduced overpotential is believed to be due to transformation into the NiOOH or $Ni(OH)_2$ phase, which can facilitate the kinetics of the water adsorption step for alkaline HER.

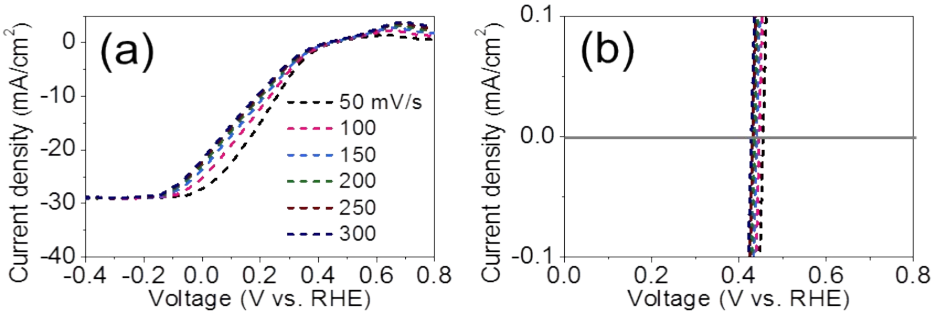

Fig. S22 (a) Scan rate-dependent illuminated LSV curves of the 3-nm-thick Ni thin film/SiO_2/Si photocathode. (b) V_{oc} characteristics.

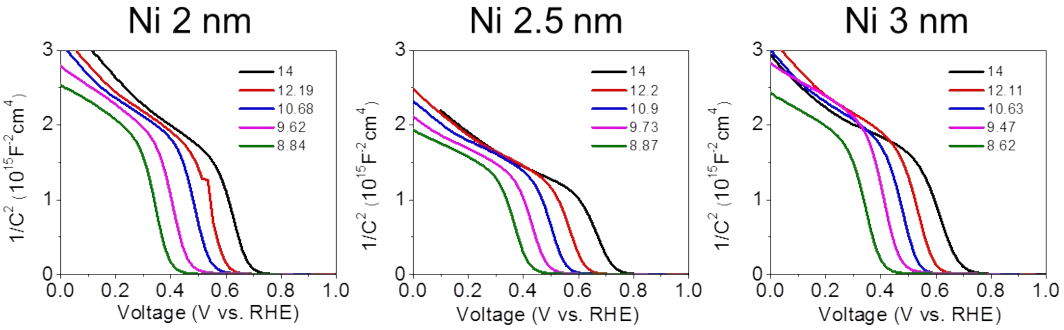

Fig. S23 Electrolyte pH-dependent V_{fb} of the Ni thin film/SiO_2/Si photocathodes with the surface-capacitive junction.

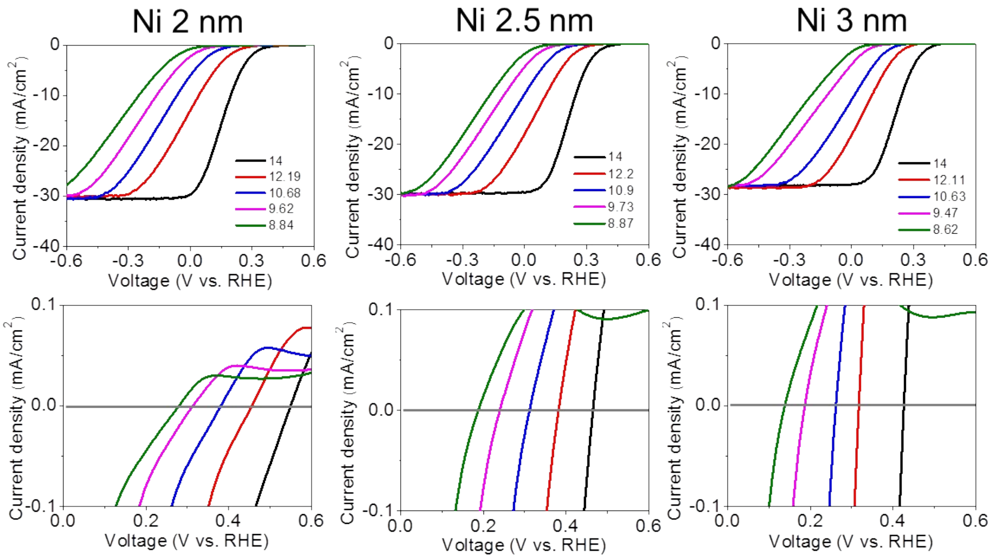

Fig. S24 (Top) Electrolyte pH-dependent illuminated LSV curves and (bottom) V_{oc} characteristics for the Si photocathodes with the surface-capacitive junctions.

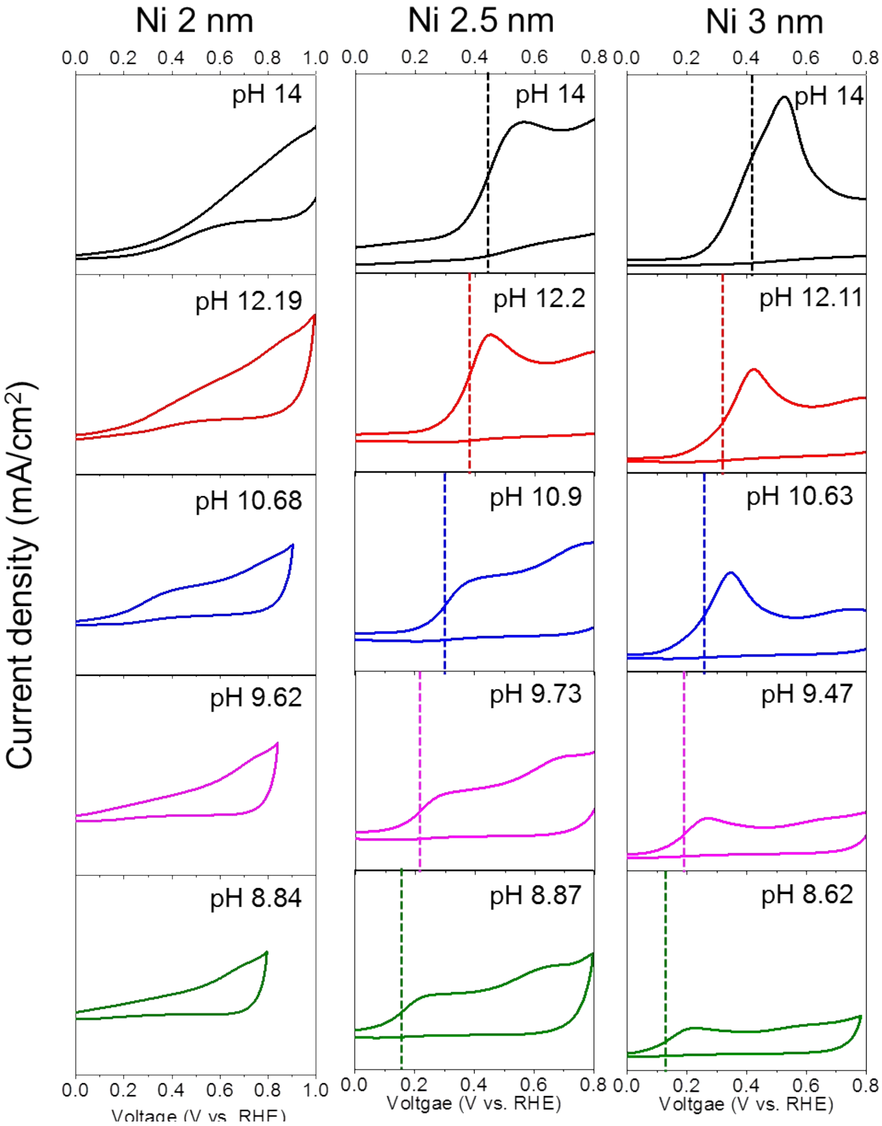

Fig. S25 Electrolyte pH-dependent dark CV curves of the Si photocathodes after PEC reaction. The dotted lines denote the electrochemical redox potential charged to the Ni thin films. In the 2 nm sample, the redox peak is not clear, so it is difficult to distinguish the electrochemical redox potential.

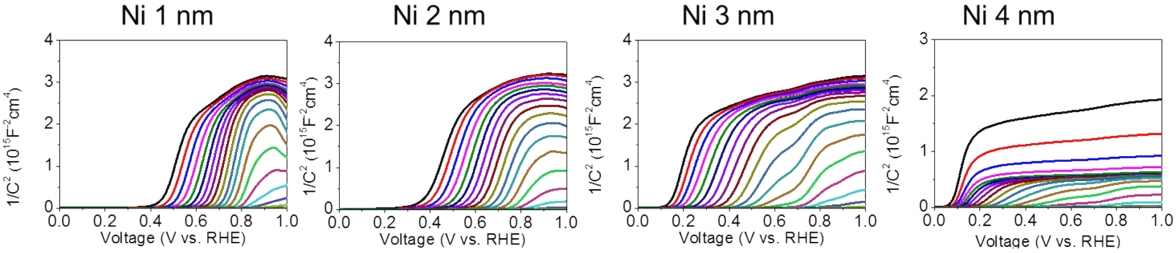

Fig. S26 Frequency-dependent V_{fb} of the Ni/SiO_2/n-Si photoanodes as a function of Ni thickness.

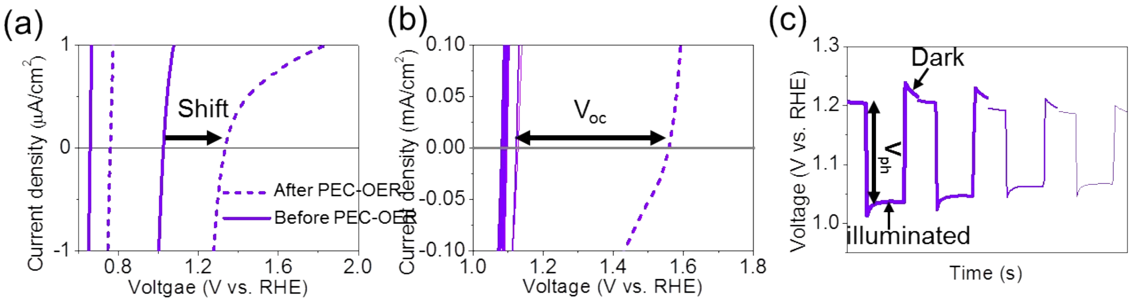

Fig. S27 (a) Characterization of the potential at zero current before and after PEC-OER. (b) V_{oc} and (c) V_{ph} results for the 3-nm-thick ultrathin Ni film/SiO_2/n-Si photoanode at various light intensities. (a) and (b) show the low current ranges of Figure 4(b) and (c) in the manuscript, respectively.

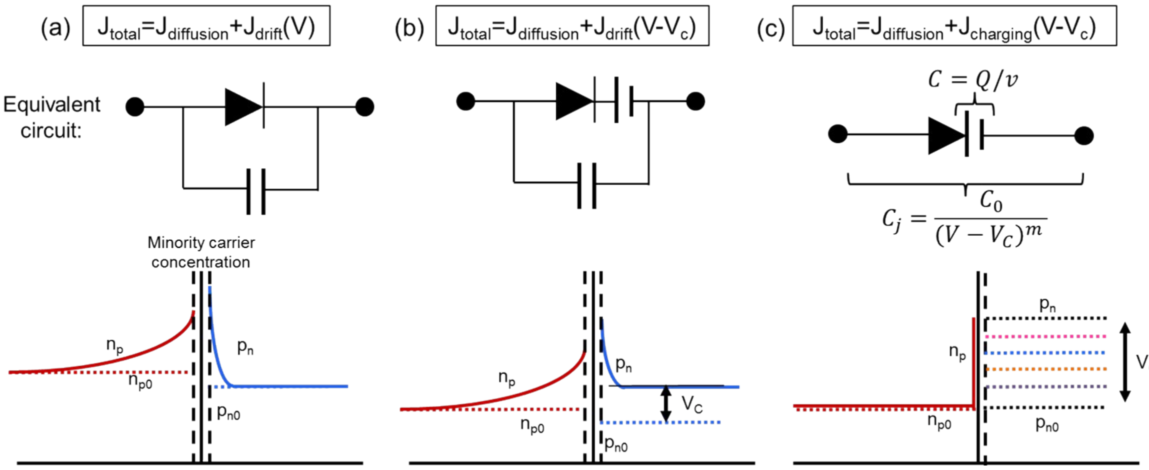

Fig. S28 Schematics describing (top) the equivalent circuits and (bottom) the boundary conditions for the three different models, (a) the classical Schottky diode model based on the net current balanced by the diffusion and the drift, (b) the model modified from (a) by adding V_C, and (c) the new model based on the net current balanced by diffusion and charging.

According to junction type, the equivalent circuit is described differently (see the top schematics of Figure S28); consequently, the boundary condition regarding the minority carrier distribution is differentiated (see the bottom schematics of Figure S28). The classical Schottky diode equation (1) denoted in the manuscript is derived from the boundary condition, where the minority carrier distribution at the edge of the depletion region under steady state follows the Boltzmann distribution, $\exp(V/nV_T)$, as depicted in Figure S28a.

Detailed derivation of the diode equation is presented in the literature.[1] When simply considering that V_C is built in the emitter region, the boundary condition is modified by adding the term $-V_C$ to the term of the applied potential, as depicted in Figure S28b. Accordingly, the modified equation (2) denoted in the manuscript can be derived.

Because there is no depletion region for the surface-capacitive junction, the boundary condition was newly established. We consider that the minority carrier at the surface-capacitive junction is distributed by the capacitance charge at the surface, as depicted in Figure S28c. Therefore, the boundary condition is derived based on the equation of the junction capacitance (C_J) that can be varied by changing the voltage in the equivalent circuit (refer to "Varicap diode"):[2]

$$C_J = \frac{C_0}{(V - V_C)^m}$$

The junction capacitance that is charged in the equivalent circuit should be identical to the local capacitance (C=Q/v), where Q is the charge, and v is the instantaneous voltage across the capacitive layer (see top schematic of Figure S28c), such that the minority carrier distribution can be denoted by the following equation:

$$C = \frac{Q}{v} = C_J = \frac{C_0}{(V - V_C)^m}$$

We can consider that Q is identical to the carrier concentration at the capacitive surface, $Q=P_n$, so

$$P_n = \frac{p_{n0} v^2}{(V - V_C)^m}$$

Based on this boundary condition, we can derive the new diode equation (3) denoted in the manuscript according to derivation of the classical diode equation.[1]

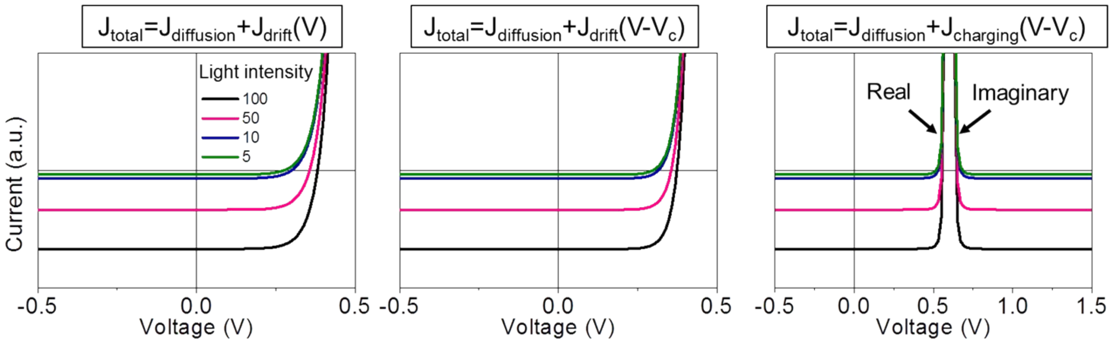

Fig. S29 I-V results for the modeling of Figure S28 at various light intensities. While V_{oc} for the Schottky diode model and the modified model is decreased as light intensity decreases, V_{oc} for the new model is unchanged.

I-V curves of new modeling (right graph) showed two symmetrical curves. One is associated with the actual PEC reaction (real part) and the other is not related to the PEC reaction (imaginary part). In the PEC reduction reaction, the left curve with the potential range lower than the charged electrochemical potential at which the reduction reaction takes place becomes the real part. The PEC oxidation reaction is reversed (see Fig. S30).

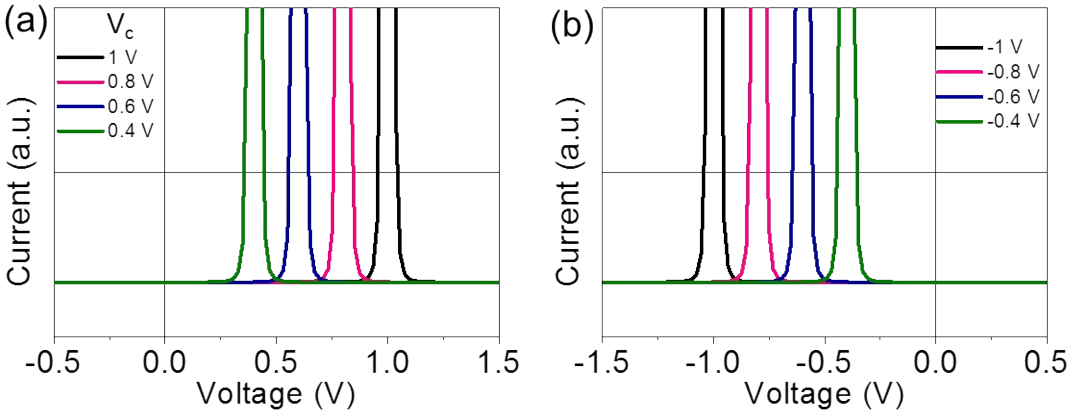

Fig. S30 I-V results for surface-capacitive junction modeling at (a) negative and (b) positive V_C. As V_C increases, I-V curves shift in the anodic direction.

Supplementary References:

1. Sah, C.-T. *Fundamentals of Solid-State Electronics* World Scientific Publishing Co. Pvt. Ltd (1991).
2. Watanabe, S. *Semiconductor Devices for Electronic Tuners* CRC Press (1991).